Pulse-shaping strategies for efficient switching of magnetic tunnel junctions by spin-orbit torque

Marco Hoffmann,[1,*] Viola Krizakova,[1] Vaishnavi Kateel,[2,3] Kaiming Cai,[2] Sebastien Couet,[2] and Pietro Gambardella[1,†]

[1] *Department of Materials, ETH Zurich, Zurich, 8093, Switzerland*
[2] *IMEC, Kapledreef 75, Leuven 3001, Belgium*
[3] *Department of Electrical Engineering ESAT, KU Leuven, Kasteelpark Arenberg 10, Leuven 3001, Belgium*

(Received 10 May 2024; accepted 30 August 2024; published 23 September 2024)

The writing energy for reversing the magnetization of the free layer in a magnetic tunnel junction (MTJ) is a key figure of merit for comparing the performances of magnetic random-access memories with competing technologies. Magnetization switching of MTJs induced by spin torques typically relies on square voltage pulses. Here, we focus on the switching of perpendicular MTJs driven by spin-orbit torque (SOT), for which the magnetization reversal process consists of sequential domain nucleation and domain-wall propagation. By performing a systematic study of the switching efficiency and speed as a function of pulse shape, we show that shaped pulses achieve up to 50% reduction of writing energy compared to square pulses without compromising the switching probability and speed. Time-resolved measurements of the tunneling magnetoresistance reveal how the switching times are strongly impacted by the pulse shape and temperature rise during the pulse. The optimal pulse shape consists of a preheating phase, a maximum amplitude to induce domain nucleation, and a lower amplitude phase to complete the reversal. Our experimental results, corroborated by micromagnetic simulations, provide diverse options to reduce the energy footprint of SOT devices in magnetic memory applications.

DOI: 10.1103/PhysRevApplied.22.034052

I. INTRODUCTION

Current-induced spin-orbit torque (SOT) switching of magnetic tunnel junctions (MTJs) has been investigated to develop fast and low-energy magnetic random-access memories (MRAM) with high endurance and speed [1–11]. In MTJ devices, the magnetization of the free layer can be manipulated by electrical currents passing either through the junction or an adjacent heavy-metal layer, inducing spin transfer torque (STT) [12,13] or SOT [14,15], respectively. SOT-induced magnetization reversal reliably reaches the subnanosecond regime [9,16–18]. However, the energy required for writing information in MTJs is a drawback for emerging SOT technologies [19,20]. Therefore, dual-pulsing schemes have been explored to decrease the switching energy consumption in MTJs, e.g., by the simultaneous application of SOT, STT, and voltage control of magnetic anisotropy (VCMA) [9,11,18,21].

The impact of self-heating due to Joule dissipation on the switching process has also been investigated [9,11,22–25]. The temperature increase ΔT of the magnetic free layer significantly reduces its perpendicular magnetic anisotropy (PMA) and thus the critical current density [26–29]. In pulsed switching, ΔT is assumed to exponentially approach its saturation value, which is proportional to the applied electrical power density [30–32]. The resultant decrease in PMA reduces the nucleation time of a domain with inverted magnetization in the free layer of the MTJ [9,33], which is the critical step to trigger SOT switching [34–36]. This insight suggests that the writing pulse may be shaped so as to optimally drive the different phases of the magnetization reversal process.

Previous works suggest that nonconventional pulsing schemes can be advantageous for several reasons. For instance, triangular pulse shapes can reduce the risk of degradation in resistive random-access memory, thanks to the improved control of current overshoots [37]. Micromagnetic simulations of STT switching of MTJs show that a current spike in the beginning of the pulse provides larger spin torque and Oersted field, such that both the switching speed and energy can be improved compared to conventional square pulses [38]. Similarly, micromagnetic simulations of SOT switching predict that using a high-amplitude pulse to initiate domain nucleation followed by a longer low-amplitude pulse for domain-wall propagation can reduce the switching energy [39]. Switching

*Contact author: Marco.Hoffmann@mat.ethz.ch
†Contact author: pietro.gambardella@mat.ethz.ch

experiments of perpendicular MTJs have shown that a reduction of the PMA during the first half of the SOT pulse leads to a concomitant reduction of the critical current [18]. Moreover, micromagnetic simulations of SOT-assisted STT switching in three-terminal MTJs yield faster and more energy-efficient magnetization reversals, if an SOT pulse is applied before the main STT pulse, such that it tilts the magnetization away from the easy-axis direction [21,40,41]. Adapting the rise and fall time of pulses can also be advantageous to improve the reliability of precessional switching induced by VCMA switching [42]. However, most experimental studies of MTJ switching so far focused on the application of square voltage pulses with a constant amplitude throughout the pulse length.

Here, we report on a systematic investigation of SOT switching of three-terminal MTJs employing diverse pulse shapes. Postpulse and time-resolved measurements reveal the switching dynamics and the critical ranges for switching voltage, energy, and pulse duration. We find that by allowing larger voltages in certain segments of the pulse, the total switching energy can be reduced by up to about 50% with respect to square pulses without significantly affecting the switching speed. Measurements performed using square, triangular, sine, and spiked voltage pulses reveal that the energy efficiency of magnetization reversal can be minimized by shaping the pulses such that the SOT and ΔT peak at approximately the same time to initiate domain nucleation while leaving enough time for the pulse to complete the reversal by SOT-driven domain-wall motion. Micromagnetic simulations that take into account the time-dependent self-heating of the free layer corroborate the experimental results.

This paper is organized as follows. The samples, experimental setup, and simulation methods are described in Sec. II. Section III elucidates the energy efficiency of different voltage pulse shapes employed for SOT switching. Subsequently, the significance of different time segments of the voltage pulse is addressed in Sec. IV. The results from our micromagnetic simulations are presented in Sec. V.

II. SAMPLES AND METHODS

A. Devices

The MTJs investigated in this work have a circular cross section with a diameter of 80 nm and comprise a free layer of $Co_{20}Fe_{60}B_{20}$ (0.9 nm) at the bottom, an MgO tunnel barrier (1.0 nm), and a reference layer of $Co_{17.5}Fe_{52.5}B_{30}$ (1.1 nm) pinned from the top by a synthetic antiferromagnetic stack made of Pt/Co multilayers. The SOT track underneath the free layer is made of β-W with resistance $R_{SOT} \approx 450\Omega$. The structure and cross section of the MTJ stack are presented in Figs. 1(a) and 1(b), respectively. More details on device fabrication are given in Refs. [8,43]. Figures 1(c) and 1(d) show the tunneling magnetoresistance

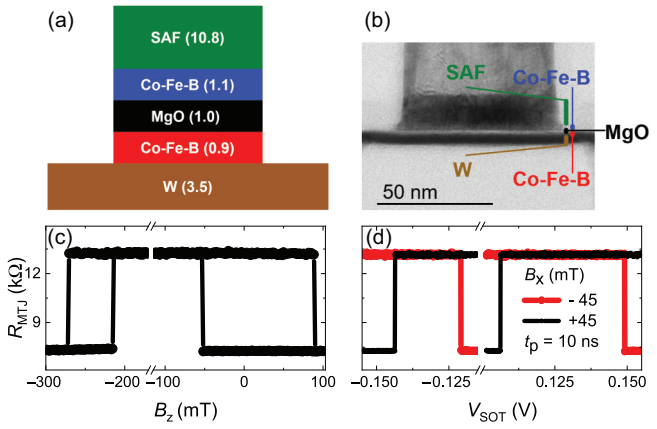

FIG. 1. (a) Schematic of the MTJ stack including, from bottom to top, the β-W SOT track, the $Co_{20}Fe_{60}B_{20}$ magnetic free layer, the MgO insulating layer, the $Co_{17.5}Fe_{52.5}B_{30}$ magnetic reference layer, a W spacer layer and the synthetic antiferromagnet made of Pt/Co layers. Numbers indicate thickness in nanometers. (b) Exemplary transmission electron microscopy image of a 60-nm-wide MTJ device. (c) TMR major loop of a representative MTJ device as a function of B_z. (d) TMR minor loops as a function of SOT voltage for both signs of B_x measured on the same device using 10-ns-long voltage pulses.

(TMR) of a representative device as a function of out-of-plane magnetic field B_z and 10-ns-long SOT voltage pulses of amplitude V_{SOT}. The resistance of the representative junction, R_{MTJ}, varies between 7.2 and 13.0 kΩ in the parallel (P) and antiparallel (AP) state, respectively.

B. Electrical measurements

In the following, we focus on the switching between the P and AP state of the MTJ, with a constant magnetic field $B_x = -45$ mT applied parallel to the current along the x direction. This field provides the symmetry breaking required for deterministic SOT switching of magnetic layers with PMA [14]. Figure 2(a) provides an overview of the experimental setup, in which an arbitrary waveform generator (AWG) with a bandwidth of 5 GHz is used to inject two separate voltage pulses into 50-Ω matched transmission lines connected to the two input terminals of the MTJs. The output waveform is measured by an oscilloscope with 10-GHz bandwidth. We perform two types of experiments: postpulse switching measurements, in which R_{MTJ} is measured several milliseconds after the voltage pulse by applying a dc voltage of 20 mV—well below any critical switching voltage—to determine the success of the switching attempt, and time-resolved switching measurements, in which R_{MTJ} is measured in real time during the application of the pulse [9]. The typical relaxation time of the temperature in our MTJ devices is of the order of a few ns [9,11]. Therefore, in either type of measurement, the temperature and magnetization are fully relaxed before every switching attempt.

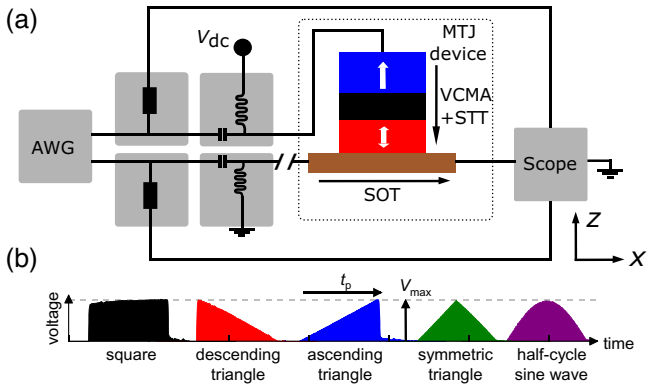

FIG. 2. (a) Schematic of the experimental setup: An arbitrary waveform generator outputs two independent voltage pulses that pass pick-off tees for raw signal investigation and triggering and bias tees before entering the input terminals of the MTJ simultaneously. The (raw) pick-off tee signals and the signal passing the MTJ are acquired on a real-time oscilloscope. (b) Different pulse shapes employed in this study: square (black), descending triangle (red), ascending triangle (blue), symmetric triangle (green), and a half-cycle sine wave (purple). t_p and V_{max} indicate the total length and maximum amplitude of the voltage pulse, respectively.

By applying simultaneously different voltages to the top terminal of the MTJ (V_{STT}) and the SOT track (V_{SOT}), the STT and SOT biases can be controlled [9]. Specifically, if $V_{STT} \approx 0.5\, V_{SOT}$, the effective voltage drop across the MTJ (V_{MTJ}) vanishes and the switching is of pure SOT nature [9]. If $V_{MTJ} \neq 0$, the switching is affected by STT and VCMA contributions. For time-resolved SOT switching, we apply a finite V_{MTJ} in order to measure R_{MTJ} during the pulse. This bias is about 30% of the critical STT switching voltage and does not cause switching by itself, but alters the critical SOT switching conditions. Thus, we can detect the change of R_{MTJ} and reveal the dynamics of the magnetization reversal in real time, while maintaining SOT-dominated switching [9,11].

The pulse shapes are affected by the limited bandwidth and stray capacitances of the electrical setup, which becomes most evident for pulse durations in the subnanosecond range. The 10% to 90% rise time of the AWG is 90 ps. To make a fair comparison between pulse shapes with sharp features [Fig. 2(b)] that are impacted differently by the finite bandwidth, we proceed in the following manner: raw pulse shapes injected to the MTJ terminals are recorded on the oscilloscope using pick-off tees. Using these raw traces, the pulse energy E_p is numerically calculated using Eq. (1) and the maximum voltage V_{max} is read off. V_{max} is defined as the maximum applied voltage for each pulse as observed in the 50-Ω matched oscilloscope, whereas a larger voltage appears on the input terminals of the MTJ device due to the impedance mismatch [9].

C. Micromagnetic simulations

We used the micromagnetic simulation software Mumax^3 [44] to model the SOT-induced switching by different pulse shapes. For this, we defined a magnetic cylinder of 80-nm diameter and 1-nm thickness in a simulation environment of $(84 \times 84 \times 1)$ nm^3 discretized into 64×64 cells in the plane. The employed magnetic parameters at room temperature are the saturation magnetization $M_{sat} = 1.1$ MA/m, the PMA energy density $K_u = 845$ kJ/m^3, and the exchange stiffness $A_{ex} = 15$ pJ/m [9]. These parameters are varied with temperature for different pulse shapes, as explained below. The Curie temperature and the damping parameter are $T_C = 750$ K and $\alpha = 0.1$, respectively. The Dzyaloshinskii-Moriya interaction is parametrized by $D = 0.15$ mJ/m^2, the in-plane magnetic field is $B_x = -45$ mT, and we simulate the P-AP transition by starting with the magnetization initially pointing along $+z$ [9].

III. SWITCHING EFFICIENCY OF DIFFERENT PULSE SHAPES

A. Postpulse measurements

We first study the SOT switching probability P_{switch} of different pulse shapes as a function of V_{max}, keeping t_p fixed to 10 or 1 ns and $V_{MTJ} = 0$. These two pulse lengths are representative of different switching regimes, dominated by thermal activation and intrinsic angular-momentum transfer, respectively [16,45]. The resulting sigmoidal curves are presented in Figs. 3(a) and 3(b). Clearly, keeping the same voltage for the entire pulse duration yields the most "voltage-efficient" switching, i.e., switching is attained at the lowest V_{max} for $P_{switch} = 50\%$. However, plotting the same switching probabilities as a function of energy

$$E_{pulse} = \int_0^{t_p} V_{pulse}^2(t)/R_{SOT}\, dt \tag{1}$$

reveals another perspective, shown in Figs. 3(c) and 3(d). Here, the function $V_{pulse}(t)$ represents the pulse shape measured by the oscilloscope. For instance, for the descending triangular pulse [Fig. 2(b)] $V_{pulse}(t)$ is close to the ideal shape

$$V_{pulse}(t) = V_{max} \cdot \left(1 - t/t_p\right) \tag{2}$$

for $t \in [0, t_p]$ and zero otherwise.

For a quantitative overview, we fit a sigmoidal function to the switching probability as a function of V_{max} and E_p and derive the critical switching voltage V_c and energy E_c where the fit crosses $P_{switch} = 50\%$. Figure 3(e) shows E_c as a function of t_p. The square pulse is the least energy efficient for any t_p. For $t_p = 10$ ns, the descending triangular and half-cycle sine wave enable magnetization reversal at about 38% reduced energy at $P_{switch} = 50\%$

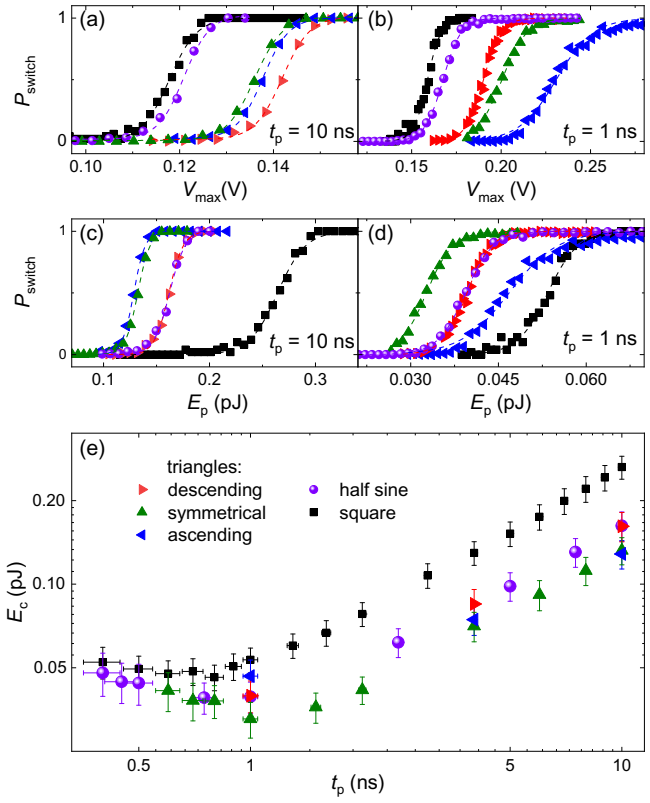

FIG. 3. SOT switching probability P_{switch} for different pulse shapes at $t_p = 10$ ns (a) and 1 ns (b) as a function of the maximum applied SOT voltage V_{max} and the corresponding pulse energy E_p in (c),(d). (e) Critical switching energy E_c as a function of t_p. All data were measured for the P-AP transition at $V_{MTJ} = 0$.

with respect to the square pulse. The ascending triangular pulse and the symmetric triangular pulse provide a better energy efficiency, with an energy reduction of 50% as compared to the square pulse. Similarly, for $t_p = 1$ ns, the square pulse is the least efficient, whereas the symmetric triangular pulse performs best, followed by the sine and descending triangular pulse. The ascending triangular pulses have become worse compared to the 10-ns case. This behavior showcases the significance of the central time interval of the pulse with respect to the end of the pulse for short pulses, which originates from the interplay of heating and SOT effects (see Sec. IV). A weak minimum in E_c can be observed around 1 ns, as expected due to the transition from the intrinsic to the thermally activated switching regime [46]. For subnanosecond pulses, the different shapes become blurred due to the finite rise time and bandwidth of the experimental setup. Consequently, the differences in switching energy also tend to vanish.

B. Time-resolved measurements

In order to time-resolve the change of R_{MTJ}, we applied $V_{MTJ} = 1.75V_{SOT}$, which induces both STT and VCMA. The selected polarity of V_{MTJ} supports the P-AP switching and corresponds to about 30% of the required pure STT switching voltage. The voltage transmitted during the pulse is normalized with respect to the averaged voltage traces in the initial and final state to yield the normalized ΔV_{sw} [9]. This quantity then reflects the time-dependent changes in the z component of the free layer's magnetization.

The input voltage and normalized time-resolved switching traces averaged over several hundreds of switching events are shown in Figs. 4(a)–4(d), respectively, for square and triangular pulses. The switching traces ΔV_{sw} consist of an initial flat part during which the magnetization of the free layer is at rest and a steadily increasing part during which the magnetization reverses. The duration of these two parts defines the average nucleation time t_0 and transition time Δt, respectively. In agreement with previous studies [9,11,34,35], we assign t_0 to the time required to nucleate an inverted domain and Δt to the time required to expand the domain until full reversal is achieved.

First, we study the switching behavior obtained by square pulses, as shown in Fig. 4(a). The square pulse with $t_p = 10$ ns and amplitude 98 mV (gray line) achieves 95% switching probability. We note that this pulse supplies a larger energy than the triangular pulses shown in Fig. 4(b). A square pulse with reduced amplitude at fixed $t_p = 10$ ns with the same energy as the triangular pulses does not result in reliable switching. The ΔV_{sw} corresponding to such a pulse, shown in Fig. 4(c), reveals that, on average, the reversal phase starts after 3 ns and spreads out over nearly half of the pulse width. The shorter square pulse with $t_p = 3.3$ ns and amplitude 159 mV (black line), on the other hand, shortens the reversal to well below 2 ns. This pulse provides the same energy as the 10-ns-long triangular pulses shown in Fig. 4(b) and achieves 99.6% switching probability, but within a shorter $t_p = 3.3$ ns.

For the three triangular pulse shapes shown in Fig. 4(b), the nominal maximum voltage is $V_{max} = 0.159$ V resulting in over-critical switching ($P_{switch} \geq 99.9\%$). In this condition, the nucleation of the inverted domain takes place around the peak of the pulse, as is evident from Fig. 4(d). The switching trace induced by the descending triangle resembles the trace of the short square pulse and completes effectively in the same time (2 ns) at lower power. The larger noise at the beginning and/or end of ΔV_{sw} observed for the triangular pulses is related to the lower current passing through the MTJ in the ascending or descending part of the pulse, which is proportional to the detected signal. Finally, real-time measurements of half-cycle sine pulses (not shown) yield switching traces comparable to the symmetric triangle, indicating a similar switching dynamics.

To resolve the switching speed in single-shot reversal events, the normalized voltage traces of individual pulses are fitted by sigmoidal functions. Then, t_0 is defined as

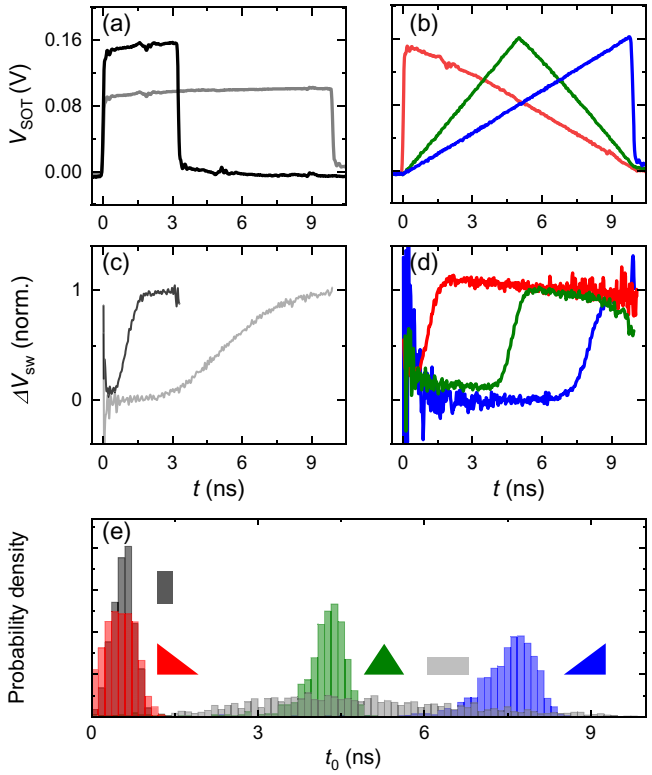

FIG. 4. Pulse shapes supplied to the SOT terminal for (a) square and (b) triangular pulses. Time-resolved normalized switching traces of (c) square and (d) triangular pulses corresponding to the P-AP transition at $B_x = -45$ mT at $V_{MTJ} = 1.75V_{SOT}$ averaged over 500 individual switching traces. The triangular pulses with $t_p = 10$ ns as well as the shortened ($t_p = 3.3$ ns, to supply the same energy) square pulse (black) were measured at the same nominal $V_{max} = 0.159$ V. The amplitude of the square voltage pulse at $t_p = 10$ ns (gray) is 98 mV and was chosen to obtain $P_{switch} = 95\%$. (e) Probability distribution of fitted nucleation times t_0 of 500 single switching events for the respective pulse shapes.

the time at which 10% of the switching is completed and Δt as the difference between the times corresponding to 90% and 10% of the switching amplitude. The statistical distributions of t_0 for different pulse shapes are presented in Fig. 4(e). In the case of the descending triangle, the reversal starts just after the pulse onset with a mean and standard deviation of 0.5 ± 0.3 ns. The distribution of t_0 is mostly symmetric around the mean. The ascending triangle, on the other hand, initiates the reversal much closer to the end of the pulse with a mean of 7.5 ± 0.6 ns. Interestingly, the distributions of t_0 for the ascending and the symmetric triangular pulse are negatively skewed. This indicates that a considerable portion of switching events is initiated before the most probable nucleation time, due the slightly overcritical conditions, thermal activation and minor contributions from VCMA and STT. The reversal of the square pulse with $t_p = 3.3$ ns (equal energy as the triangular pulses) starts at around 0.5 ± 0.2 ns, similar to the descending triangle. On the other hand, square pulses of lower amplitude with $t_p = 10$ ns present a much broader and delayed t_0 distribution, with a mean value of 4.8 ± 1.9 ns and the successful switching attempts spread over the entire pulse length. This explains why the averaged switching trace in Fig. 4(c) appears slower compared to $t_p = 3.3$ ns.

The mean values and standard deviations of Δt for all pulse shapes (not shown) do not reveal significant variations and fall into the range 1.0 ± 0.2 ns. Therefore, the domain-wall propagation behavior is not largely influenced by the pulse shape. This observation is consistent with prior work on three-terminal MTJs, where only weak changes of Δt were reported as a function of V_{SOT} and V_{MTJ} [9,11,17]. This behavior can be explained if the domain-wall propagation velocity is already close to saturation for the range of V_{SOT} required to trigger domain nucleation and initiate the reversal process [47–49]. We also note that resolving differences in Δt below 0.5 ns is hindered by the limited bandwidth of our setup.

Overall, the statistical distributions of t_0 and Δt indicate that, for the same E_{pulse}, pulse shaping can lead to significant advantages not only in terms of energy efficiency but also in terms of switching speed. The different efficiencies and t_0 distributions for the above-presented pulse shapes can be explained by the temperature-activated nature of the domain nucleation process and the different timescales of Joule heating and SOT. Whereas the strength of the torque varies simultaneously with the applied voltage, the temperature increase varies as $\Delta T \propto 1 - e^{-t/\tau}$, where $\tau \approx 1.5 - 4.0$ ns is a thermal time constant that depends on device size [9,11,22,28]. Maximum efficiency and speed of the reversal process are achieved when ΔT and the SOT peak at approximately the same time. Our modeling in Sec. V further supports this interpretation, showing that the symmetric and ascending triangular pulses lead to higher device temperatures coinciding with larger SOT. In the next section, this reasoning is further exemplified by studying the relevance of each interval of the pulse in a systematic way using square voltage pulses with superimposed delayed voltage spikes.

IV. SWITCHING EFFICIENCY OF SQUARE PULSES WITH DELAYED VOLTAGE SPIKES

A. Postpulse measurements

To understand the relevance of different segments of the pulses with total duration of 10 or 1 ns, we study here the switching characteristics of two superposed square pulses with a variable delay. We used pulses with a square base amplitude V_{base} and length t_p featuring a square spike of double the base amplitude ($V_{max} = 2V_{base}$) and duration $t_{spike} = 0.1t_p$. The delay t_{delay} of the spike with respect to

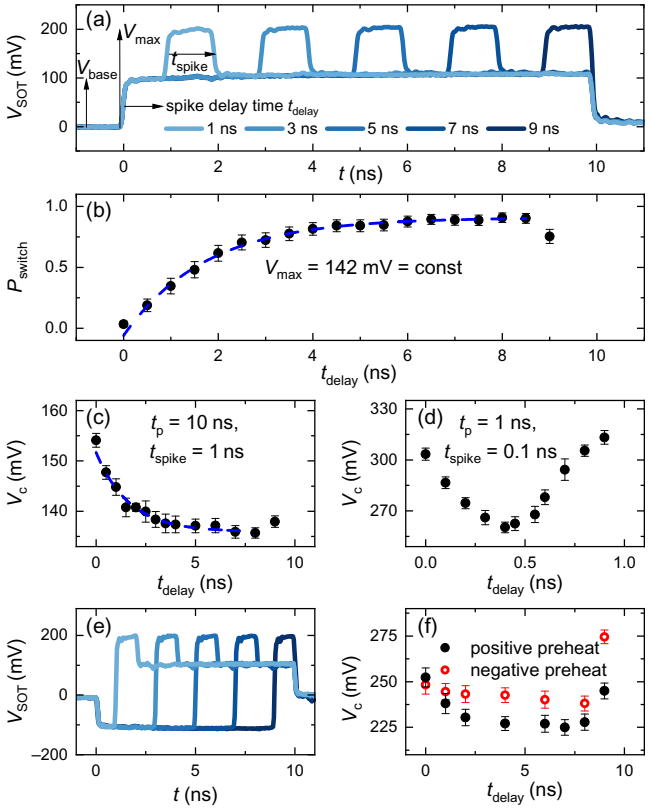

FIG. 5. (a) Pulse shapes consisting of a square baseline (V_{base}) with an overlapping voltage spike of duration $t_{spike} = 1$ ns and amplitude $V_{max} = 2V_{base}$ delayed by t_{delay}. Pulses of total duration $t_p = 10$ ns and varying t_{delay} are shown. (b) Switching probability as a function of spike delay at a fixed applied voltage fit by an exponential function shown as the dashed line. (c) Critical applied maximal voltage V_c vs t_{delay} as determined from the sigmoid curve fits to the voltage sweeps (not shown) and the exponential fit (dashed line) (d) V_c for the same pulse shape with $t_p = 1$ ns, $t_{spike} = 0.1$ ns, and $V_{spike} = 2V_{base}$ for different t_{delay}. (e) Pulse shapes with a negative preheating phase before the spike. Here, t_{delay} marks the time at which the polarity of the voltage switches. (f) Comparison of the t_{delay} dependence of V_c for a preheating phase with supportive (black) and opposing (red) SOT in a different device with modified critical conditions. All data were recorded for the P-AP switch at $V_{MTJ} = 0$ and $B_x = -45$ mT.

the base pulse was varied between 0 and $0.9t_p$ [Fig. 5(a)]. In this manner, the total injected angular momentum and pulse energy is constant for different t_{delay}.

At $t_p = 10$ ns and fixed voltage amplitude, the pure SOT switching probability measured over 500 events increases for longer t_{delay} [Fig. 5(b)]. This change is most pronounced during the first few nanoseconds and saturates for longer t_{delay}. An exponential fit of P_{switch} yields a characteristic timescale of 2.0 ± 0.3 ns resulting in 95% switching probability after 6 ns. This timescale is similar to the self-heating relaxation time reported in MTJ devices [9,22,28]. However, if the spike ends simultaneously with the base pulse, a decrease in switching probability is noticeable. As Δt is about as long as the remaining pulse time after the spike in this case, the magnetization reversal cannot complete reliably. Also V_c is influenced by t_{delay} [Fig. 5(c)], decreasing exponentially with t_{delay} until $t_p - t_{spike} = 9$ ns, for which a slight increase in V_c is observed, consistently with the reduction of P_{switch} reported above. This trend is in line with the increased energy efficiencies of the symmetric and ascending triangular pulses described in Fig. 3(c).

In contrast, at $t_p = 1$ ns V_c in Fig. 5(d) has a minimum approximately at the center of the pulse. In accordance with Fig. 3(d), these results demonstrate that the free layer is easiest to switch when the highest driving voltages appear neither in the beginning nor in the end of the pulse. This behavior is consistent with the requirement of a preheating phase leading to thermally activated domain nucleation and a subsequent domain-expansion phase driven by SOT.

To distinguish between the action of torque and self-heating, we further investigate a preheating phase of duration t_{delay} with inverted voltage $-V_{base}$ and inverted torques [Fig. 5(e)]. The resulting V_c vs t_{delay} is presented for a preheating phase with either supportive and opposing SOT in Fig. 5(f). Whereas the preheating phase with opposing torque qualitatively resembles the preceding results, the decrease of V_c is not as pronounced as for the supportive torque. Thus, the switching success of the voltage spike is not solely given by the self-heating effect of the preheating phase. Instead, the difference of the two data sets in Fig. 5(f) implies that the SOT also plays a role in triggering the reversal.

B. Time-resolved measurements

To investigate whether the discontinuity caused by the voltage spike makes the two-phase reversal process less uniform, time-resolved measurements were performed: Figure 6(a) presents averaged switching traces for the pulse shapes shown in Fig. 5(a) at constant $V_{max} = V_{spike} = 130$ mV and $V_{MTJ} = 2V_{SOT}$. Due to the trend illustrated in Fig. 5(b), these conditions are undercritical for $t_{delay} = 0$ ns yielding a switching probability of 15%. For longer t_{delay}, reliable switching is achieved. For higher driving voltages, the magnetization dynamics would be accelerated and the differences between traces more subtle.

The averaged switching traces reveal close similarities with the ones presented in Fig. 4(d): the part of the pulse featuring the largest voltage amplitudes, i.e., the spikes here, trigger the reversal process in critical conditions. The reversal initiates on average within the spike. Therefore, the switching traces appear to be offset in time approximately by the respective differences in t_{delay}, but are otherwise similar to each other. A mild trend is revealed by analyzing how the difference $t_0 - t_{delay}$ depends on t_{delay}. This quantity measures how soon the spike succeeds in

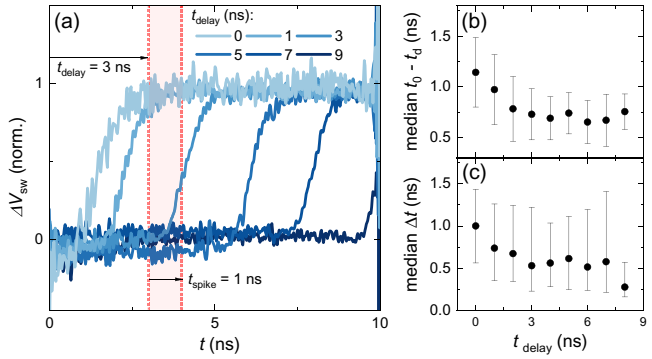

FIG. 6. (a) Time-resolved switching traces for the pulse shapes presented in Fig. 5(a) averaged over approximately equal to 500 events. The shaded area indicates the duration of the spike with $t_{delay} = 3$ ns. (b) Dependence of the median nucleation time t_0 offset by the corresponding t_{delay} and (c) Δt on t_{delay}, as determined by sigmoid fits to the individual switching events. The error bars span lower and upper quartiles of the distributions. All data were recorded at $V_{MTJ} = 2V_{SOT}$, $t_p = 10$ ns, and $t_{spike} = 1$ ns.

initiating the reversal. The medians of $t_0 - t_{delay}$ and Δt determined by fits to the successful individual switching events that complete within t_p are presented for several t_{delay} in Figs. 6(b) and 6(c), respectively. For longer t_{delay}, we find shorter intervals between spike onset and nucleation time. This decrease reflects the same trend as observed for V_c in Fig. 5(c) and may be understood by considering that t_0 is a measure of the energy barrier that needs to be overcome in the reversal process [35]. The energy barrier and thus t_0 are diminished thanks to the higher temperature reached for longer t_{delay}. A similar, even more subtle trend is obtained for the medians of Δt [cf. Fig. 6(c)]. Therefore, higher temperatures appear to enhance the reversal speed, consistently with models of domain-wall propagation in the presence of a pinning potential [35], leading to shorter Δt. Overall, also the time-resolved switching data evidence the influence of temperature, supporting the scenario in which pulse spikes occurring after a preheating phase of a few nanoseconds facilitate the switching.

V. MICROMAGNETIC MODEL INCLUDING SELF-HEATING

To incorporate the temperature dynamics induced by different pulse shapes into the micromagnetic model, we assume that the saturation magnetization M_S scales with temperature as $M_S = M_{S,0}(1 - T/T_C)^{\beta}$, where $M_{S,0} = 1.83$ MA/m, $T_C = 750$ K is the Curie temperature, and $\beta = 1$ the critical exponent. The magnetic anisotropy $K_u(T)$ (845 kJ/m^3 at 300 K) and exchange stiffness $A_{ex}(T)$ (15 pJ/m at 300 K) scale like $K_0 (M_S(T)/M_{S0})^p$ and $A_{ex0} (M_S(T)/M_{S0})^q$ with $p = 2.5$ and $q = 1.7$, respectively. More details are found in the literature [9,50]. The final temperature induced by self-heating is proportional to the square of the current density [30], assuming a negligible change in resistance. The system requires a finite time to equilibrate the temperature while heat is dissipated via the adjoining layers and the material surrounding the MTJ pillar. We describe the continuous release of heat into the environment by an exponential decay with an effective relaxation time $\tau = 2.5$ ns [9,31] convoluted with self-heating:

$$c_{eff}\Delta T(t) = \int_0^t R_{SOT} A_{SOT}^2 j_{SOT}^2(t') e^{-\frac{t-t'}{\tau}} dt', \qquad (3)$$

where c_{eff} and A_{SOT} are the effective heat capacity of the MTJ and the cross section of the SOT track, respectively, and $j_{SOT}(t)$ is the injected current density.

Using this approach, we simulate pure SOT switching induced by the pulse shapes shown in Figs. 7(a) and 7(b). The resulting transient dependencies of temperature and K_u are given in Figs. 7(c)–7(f). By varying j_{SOT}, we extract the lowest amplitude j_c at which successful switching occurs. For different pulse shapes, j_c can be converted to the corresponding energy E_c using Eq. (1) for $t_p = 10$ ns and 1 ns, as shown in Figs. 7(g) and 7(h), respectively. The simulation results for E_c and the different pulse shapes are plotted considering a constant and a variable temperature scenario. Generally, we find good agreement with the energy efficiency of the pulse shapes investigated experimentally [Fig. 3(e)]. In the thermally activated regime ($t_p = 10$ ns), the reduction in E_c is more pronounced than for 1 ns. The descending triangle provides its largest SOT instantly after the onset of the pulse. Therefore, it benefits the least from the temperature increase that follows only at later times.

The simulated j_c for the pulses shown in Fig. 7(b) are plotted as a function of t_{delay} in Fig. 7(i). These values reflect the experimental observations with the exponentially saturating decrease of j_c due to preheating and the mild increase due to the finite reversal completion time. Without the transient variation of temperature and anisotropy, the variation of j_c with t_{delay} disappears, as shown in Fig. 7(j). Overall, the simulations corroborate our interpretation of the experimental trends and confirm that the duration of the preheating phase and of the domain-wall propagation phase determine the optimal pulse shape for a given maximum current amplitude.

VI. CONCLUSIONS

We investigated the SOT switching induced by shaped voltage pulses in three-terminal MTJs using postpulse and time-resolved measurements as well as micromagnetic simulations. We found that modulating the voltage amplitude over the pulse duration can induce substantial

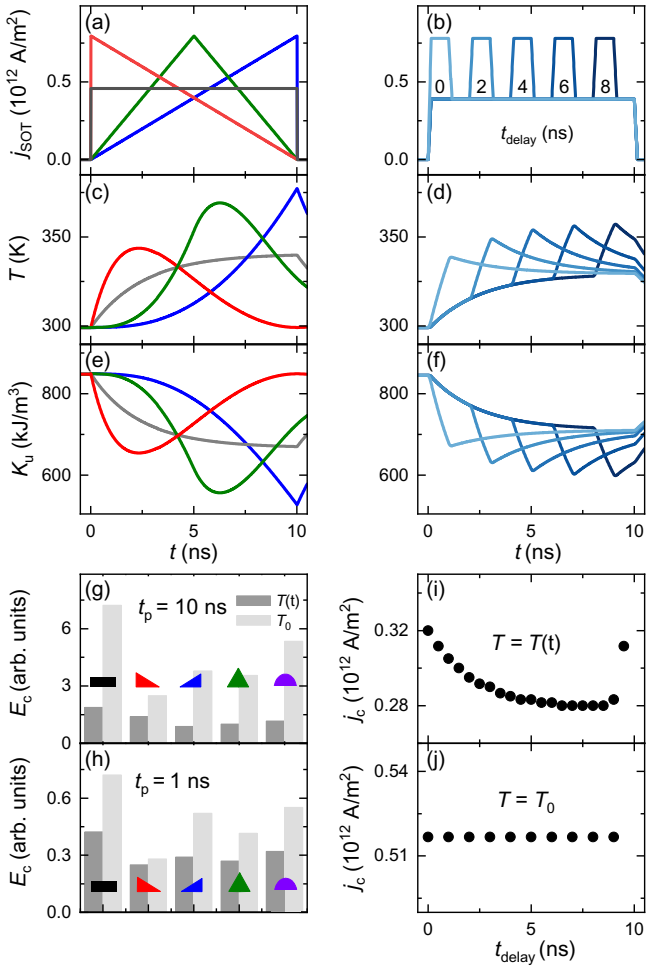

FIG. 7. (a) Single pulses and (b) spiked pulses with varying t_{delay} together with their corresponding transient evolution of (c),(d) temperature and (e),(f) uniaxial anisotropy. Critical switching energy for the different pulse shapes at (g) $t_p = 10$ ns and (h) 1 ns as determined from the lowest current density that achieves switching j_c. The simulations are performed for a time-dependent temperature given by Eq. (3) (dark gray) and constant temperature $T_0 = 300$ K (light gray). Critical current density j_c for the square pulse shapes with amplitude spikes as a function of t_{delay} (i) with and (j) without temperature variation.

gains in energy efficiency without necessarily degrading the switching speed. In the thermally activated regime at $t_p = 10$ ns, the ascending and symmetric triangular pulse are the most efficient, indicating large voltage amplitudes between the center and the end of the pulse favor the reversal process. This finding is rationalized by a preheating effect: the initial part of the pulse raises the device temperature and lowers the domain nucleation barrier, followed by a voltage increase that induces a strong SOT and achieves the nucleation. Upon approaching the intrinsic regime at $t_p = 1$ ns, the symmetric triangular pulse is the most efficient, while the descending triangular pulse is more efficient than the ascending triangle. Hence, it is more favorable to provide large voltages around the center of the pulse. This trend can be explained by considering that, in the intrinsic limit, the strongest voltage should be provided at the beginning of the pulse in order to trigger domain nucleation, followed by a smaller voltage to drive the domain expansion. The observations for both switching regimes are confirmed by systematically shifting a pulse spike on top of a square base pulse.

Time-resolved measurements demonstrate that the largest voltage amplitude within a given pulse trigger domain nucleation and initiate the magnetization reversal at critical switching conditions. The statistical distributions of the nucleation time t_0 are strongly affected by the pulse shape. Near the critical switching voltage, the total switching time is dominated by t_0. On the other hand, expanding the nucleated inverted domain through the entire free layer requires a finite time Δt (here approximately equal to 0.8 ± 0.4 ns), which is only mildly impacted by changing the pulse shape and temperature of the device. Consequently, the optimal efficiency and switching speed are achieved when the largest voltage amplitude is applied near the middle of the pulse and earlier than Δt before the pulse terminates.

Micromagnetic simulations implementing time-dependent SOT proportional to the pulse shape $V(t)$ and a simple dynamic temperature relaxation model based on self-heating reproduce the experimental observations. The simulations performed for different pulse shapes and durations reveal the characteristic timescale on which the device heats up and interplay between SOT and thermally activated dynamics, which is key to optimize the pulse shape and duration to achieve maximum switching efficiency on the nanosecond timescale.

In practical terms, the switching speed and energy are both optimized by a symmetric triangular pulse saving about 39% (50%) with respect to a square pulse lasting 1 ns (10 ns). Additional measurements show that a sine-shaped pulse, as commonly used in radiofrequency electronics, has qualitatively similar effects to the symmetric triangle and saves about 25% in switching energy with respect to a square pulse. Our work shows how shaped pulses can contribute to lowering the critical switching energy of MTJs in memory devices. Future investigations may take advantage of shaped pulses to implement nonbinary switching algorithms, as required, e.g., in probabilistic and neuromorphic computing architectures [51–53].

ACKNOWLEDGMENTS

This project has received funding from the European Union's Horizon 2020 research and innovation programme under the Marie Skłodowska-Curie Grant Agreement No. 955671. This work was further supported by the Swiss National Science Foundation (Grant No. 200020_200465)

and IMEC's IIAP industrial partner affiliation program on SOT-MRAM.

[1] A. Manchon, J. Železný, I. M. Miron, T. Jungwirth, J. Sinova, A. Thiaville, K. Garello, and P. Gambardella, Current-induced spin-orbit torques in ferromagnetic and antiferromagnetic systems, Rev. Mod. Phys. **91**, 035004 (2019).

[2] L. Liu, O. J. Lee, T. J. Gudmundsen, D. C. Ralph, and R. A. Buhrman, Current-induced switching of perpendicularly magnetized magnetic layers using spin torque from the spin Hall effect, Phys. Rev. Lett. **109**, 096602 (2012).

[3] C. F. Pai, L. Liu, Y. Li, H. W. Tseng, D. C. Ralph, and R. A. Buhrman, Spin transfer torque devices utilizing the giant spin Hall effect of tungsten, Appl. Phys. Lett. **101**, 122404 (2012).

[4] M. Cubukcu, O. Boulle, M. Drouard, K. Garello, C. Onur Avci, I. Mihai Miron, J. Langer, B. Ocker, P. Gambardella, and G. Gaudin, Spin-orbit torque magnetization switching of a three-terminal perpendicular magnetic tunnel junction, Appl. Phys. Lett. **104**, 042406 (2014).

[5] S. V. Aradhya, G. E. Rowlands, J. Oh, D. C. Ralph, and R. A. Buhrman, Nanosecond-timescale low energy switching of in-plane magnetic tunnel junctions through dynamic Oersted-field-assisted spin Hall effect, Nano Lett. **16**, 5987 (2016).

[6] S. Fukami, T. Anekawa, A. Ohkawara, C. Zhang, and H. Ohno, in *IEEE Symposium on VLSI Technology* (IEEE, Honolulu, HI, USA, 2016), p. 1, https://ieeexplore.ieee.org/document/7573379.

[7] M. Cubukcu, O. Boulle, N. Mikuszeit, C. Hamelin, T. Brächer, N. Lamard, M.-C. Cyrille, L. Buda-prejbeanu, K. Garello, I. M. Miron, O. Klein, G. D. Loubens, V. V. Naletov, J. Langer, B. Ocker, P. Gambardella, and G. Gaudin, Ultra-fast perpendicular spin–orbit torque MRAM, IEEE Trans. Magn. **54**, 1 (2018).

[8] K. Garello, F. Yasin, S. Couet, L. Souriau, J. Swerts, S. Rao, S. Van Beek, W. Kim, E. Liu, S. Kundu, D. Tsvetanova, K. Croes, N. Jossart, E. Grimaldi, M. Baumgartner, D. Crotti, A. Fumémont, P. Gambardella, and G. Kar, in *IEEE Symp. VLSI Circ.* (IEEE, Honolulu, HI, USA, 2018), p. 81, https://ieeexplore.ieee.org/document/8502269.

[9] E. Grimaldi, V. Krizakova, G. Sala, F. Yasin, S. Couet, G. Sankar Kar, K. Garello, and P. Gambardella, Single-shot dynamics of spin–orbit torque and spin transfer torque switching in three-terminal magnetic tunnel junctions, Nat. Nano **15**, 111 (2020).

[10] T. Endoh, H. Honjo, K. Nishioka, and S. Ikeda, in *IEEE Symp. VLSI Techn.* (IEEE, Honolulu, HI, USA, 2020), p. 1, https://ieeexplore.ieee.org/abstract/document/9265042.

[11] V. Krizakova, E. Grimaldi, K. Garello, G. Sala, S. Couet, G. S. Kar, and P. Gambardella, Interplay of voltage control of magnetic anisotropy, spin-transfer torque, and heat in the spin-orbit-torque switching of three-terminal magnetic tunnel junctions, Phys. Rev. Appl. **15**, 054055 (2021).

[12] D. Ralph and M. Stiles, Spin transfer torques, J. Magn. Magn. Mat. **320**, 1190 (2008).

[13] A. Brataas, A. D. Kent, and H. Ohno, Current-induced torques in magnetic materials, Nat. Mat. **11**, 372 (2012).

[14] I. M. Miron, K. Garello, G. Gaudin, P.-J. Zermatten, M. V. Costache, S. Auffret, S. Bandiera, B. Rodmacq, A. Schuhl, and P. Gambardella, Perpendicular switching of a single ferromagnetic layer induced by in-plane current injection, Nature **476**, 189 (2011).

[15] K. Garello, I. M. Miron, C. O. Avci, F. Freimuth, Y. Mokrousov, S. Blügel, S. Auffret, O. Boulle, G. Gaudin, and P. Gambardella, Symmetry and magnitude of spin-orbit torques in ferromagnetic heterostructures, Nat. Nano **8**, 587 (2013).

[16] K. Garello, C. O. Avci, I. M. Miron, M. Baumgartner, A. Ghosh, S. Auffret, O. Boulle, G. Gaudin, and P. Gambardella, Ultrafast magnetization switching by spin-orbit torques, Appl. Phys. Lett. **105**, 212402 (2014).

[17] V. Krizakova, K. Garello, E. Grimaldi, G. S. Kar, and P. Gambardella, Field-free switching of magnetic tunnel junctions driven by spin–orbit torques at sub-ns timescales, Appl. Phys. Lett. **116**, 232406 (2020).

[18] Y. C. Wu, K. Garello, W. Kim, M. Gupta, M. Perumkunnil, V. Kateel, S. Couet, R. Carpenter, S. Rao, S. Van Beek, K. K. Vudya Sethu, F. Yasin, D. Crotti, and G. S. Kar, Voltage-gate-assisted spin-orbit-torque magnetic random-access memory for high-density and low-power embedded applications, Phys. Rev. Appl. **15**, 064015 (2021).

[19] V. Krizakova, M. Hoffmann, V. Kateel, S. Rao, S. Couet, G. S. Kar, K. Garello, and P. Gambardella, Tailoring the switching efficiency of magnetic tunnel junctions by the fieldlike spin-orbit torque, Phys. Rev. Appl. **18**, 044070 (2022).

[20] E. Y. Vedmedenko, R. K. Kawakami, D. D. Sheka, P. Gambardella, A. Kirilyuk, A. Hirohata, C. Binek, O. Chubykalo-Fesenko, S. Sanvito, B. J. Kirby, J. Grollier, K. Everschor-Sitte, T. Kampfrath, C. Y. You, and A. Berger, The 2020 magnetism roadmap, J. Phys. D: Appl. Phys. **53**, 453001 (2020).

[21] S. Pathak, C. Youm, and J. Hong, Impact of spin-orbit torque on spin-transfer torque switching in magnetic tunnel junctions, Sci. Rep. **10**, 2799 (2020).

[22] A. Chavent, C. Ducruet, C. Portemont, L. Vila, J. Alvarez-Hérault, R. Sousa, I. L. Prejbeanu, and B. Dieny, Steady state and dynamics of joule heating in magnetic tunnel junctions observed via the temperature dependence of RKKY coupling, Phys. Rev. Appl. **6**, 034003 (2016).

[23] G. Mihajlović, N. Smith, T. Santos, J. Li, M. Tran, M. Carey, B. D. Terris, and J. A. Katine, Origin of the Resistance-Area-Product Dependence of Spin-Transfer-Torque Switching in Perpendicular Magnetic Random-Access Memory Cells, Phys. Rev. Appl. **13**, 024004 (2020).

[24] M. Goto, R. Kobayashi, R. Okuno, T. Mizuno, T. Yamane, N. Degawa, T. Suzuki, A. Shimura, S. Aoki, J. Urabe, S. Hara, H. Nomura, and Y. Suzuki, Junction size dependence of the heat controlled magnetic anisotropy in magnetic tunnel junctions, Appl. Phys. Exp. **15**, 13001 (2022).

[25] T. Hadámek, N. P. Jørstad, R. L. de Orio, W. Goes, S. Selberherr, and V. Sverdlov, A comprehensive study of temperature and its effects in SOT-MRAM devices, Micromachines **14**, 1581 (2023).

[26] A. Yamaguchi, S. Nasu, H. Tanigawa, T. Ono, K. Miyake, K. Mibu, and T. Shinjo, Effect of joule heating in current-driven domain wall motion, Appl. Phys. Lett. **86**, 012511 (2004).

[27] C.-Y. You, I. M. Sung, and B.-K. Joe, Analytic expression for the temperature of the current-heated nanowire for the current-induced domain wall motion, Appl. Phys. Lett. **89**, 222513 (2006).

[28] C. Papusoi, R. Sousa, J. Herault, I. L. Prejbeanu, and B. Dieny, Probing fast heating in magnetic tunnel junction structures with exchange bias, New J. Phys. **10**, 103006 (2008).

[29] T. Hadámek, S. Fiorentini, M. Bendra, J. Ender, R. de Orio, W. Goes, S. Selberherr, and V. Sverdlov, Temperature increase in STT-MRAM at writing: A fully three-dimensional finite element approach, Solid-State Electron. **193**, 108269 (2022).

[30] R. C. Sousa, I. L. Prejbeanu, D. Stanescu, B. Rodmacq, O. Redon, B. Dieny, J. Wang, and P. P. Freitas, Tunneling hot spots and heating in magnetic tunnel junctions, J. Appl. Phys. **95**, 6783 (2004).

[31] K.-J. Kim, J.-C. Lee, S.-B. Choe, and K.-H. Shin, Joule heating in ferromagnetic nanowires: Prediction and observation, Appl. Phys. Lett. **92**, 192509 (2008).

[32] S. Fukami, M. Yamanouchi, H. Honjo, K. Kinoshita, K. Tokutome, S. Miura, S. Ikeda, N. Kasai, and H. Ohno, Electrical endurance of Co/Ni wire for magnetic domain wall motion device, Appl. Phys. Lett. **102**, 222410 (2013).

[33] N. Strelkov, A. Chavent, A. Timopheev, R. C. Sousa, I. L. Prejbeanu, L. D. Buda-Prejbeanu, and B. Dieny, Impact of joule heating on the stability phase diagrams of perpendicular magnetic tunnel junctions, Phys. Rev. B **98**, 214410 (2018).

[34] M. Baumgartner, K. Garello, J. Mendil, C. O. Avci, E. Grimaldi, C. Murer, J. Feng, M. Gabureac, C. Stamm, Y. Acremann, S. Finizio, S. Wintz, J. Raabe, and P. Gambardella, Spatially and time-resolved magnetization dynamics driven by spin-orbit torques, Nat. Nano **12**, 980 (2017).

[35] G. Sala, J. Meyer, A. Flechsig, L. Gabriel, and P. Gambardella, Deterministic and stochastic aspects of current-induced magnetization reversal in perpendicular nanomagnets, Phys. Rev. B **107**, 214447 (2023).

[36] M. Martinez, L. Torres, N. Perez, M. A. Hernandez, V. Raposo, and S. Moretti, Universal chiral-triggered magnetization switching in confined nanodots, Sci. Rep. **5**, 10156 (2015).

[37] S. Lee, J. Song, D. Lee, J. Woo, E. Cha, and H. Hwang, Effect of AC pulse overshoot on nonlinearity and reliability of selectorless resistive random access memory in AC pulse operation, Solid-State Electron. **104**, 70 (2015).

[38] S. Pathak, J. Cha, K. Jo, H. Yoon, and J. Hong, Fast and efficient STT switching in MTJ using additional transient pulse current, Appl. Phys. Lett. **110**, 232401 (2017).

[39] T. Jin, C. Ang, X. Wang, W. Siang Lew, and S. Piramanayagam, Efficient spin–orbit torque magnetization switching by reducing domain nucleation energy, J. Magn. Magn. Mat. **562**, 169759 (2022).

[40] W. Cai, K. Shi, Y. Zhuo, D. Zhu, Y. Huang, J. Yin, K. Cao, Z. Wang, Z. Guo, Z. Wang, G. Wang, and W. Zhao, Sub-ns field-free switching in perpendicular magnetic tunnel junctions by the interplay of spin transfer and orbit torques, IEEE Electron Dev. Lett. **42**, 704 (2021).

[41] C. Yoshida, T. Tanaka, T. Ataka, M. Hoshina, and A. Furuya, Field-free reliable magnetization switching in a three-terminal perpendicular magnetic tunnel junction via spin-orbit torque, spin-transfer torque, and voltage-controlled magnetic anisotropy, J. Phys. D: Appl. Phys. **55**, 365003 (2022).

[42] T. Yamamoto, T. Nozaki, H. Imamura, Y. Shiota, T. Ikeura, S. Tamaru, K. Yakushiji, H. Kubota, A. Fukushima, Y. Suzuki, and S. Yuasa, Write-error reduction of voltage-torque-driven magnetization switching by a controlled voltage pulse, Phys. Rev. Appl. **11**, 014013 (2019).

[43] K. Garello, F. Yasin, and G. S. Kar, in *2019 IEEE 11th International Memory Workshop (IMW)* (IEEE, Monterey, CA, USA, 2019), p. 1, https://ieeexplore.ieee.org/document/8739466.

[44] A. Vansteenkiste, J. Leliaert, M. Dvornik, M. Helsen, F. Garcia-Sanchez, and B. Van Waeyenberge, The design and verification of MuMax3, AIP Adv. **4**, 107133 (2014).

[45] D. Bedau, H. Liu, J. Z. Sun, J. A. Katine, E. E. Fullerton, S. Mangin, and A. D. Kent, Spin-transfer pulse switching: From the dynamic to the thermally activated regime, Appl. Phys. Lett. **97**, 262502 (2010).

[46] G. Sala and P. Gambardella, Ferrimagnetic dynamics induced by spin-orbit torques, Adv. Mat. Interf. **9**, 2201622 (2022).

[47] E. Martinez, S. Emori, N. Perez, L. Torres, and G. S. D. Beach, Current-driven dynamics of Dzyaloshinskii domain walls in the presence of in-plane fields: Full micromagnetic and one-dimensional analysis, J. Appl. Phys. **115**, 213909 (2014).

[48] N. Mikuszeit, O. Boulle, I. M. Miron, K. Garello, P. Gambardella, G. Gaudin, and L. D. Buda-Prejbeanu, Spin-orbit torque driven chiral magnetization reversal in ultrathin nanostructures, Phys. Rev. B **92**, 144424 (2015).

[49] M. Baumgartner and P. Gambardella, Asymmetric velocity and tilt angle of domain walls induced by spin-orbit torques, Appl. Phys. Lett. **113**, 242402 (2018).

[50] K.-M. Lee, J. W. Choi, J. Sok, and B.-C. Min, Temperature dependence of the interfacial magnetic anisotropy in W/CoFeB/MgO, AIP Adv. **7**, 065107 (2017).

[51] M.-H. Wu, I.-T. Wang, M.-C. Hong, K.-M. Chen, Y.-C. Tseng, J.-H. Wei, and T.-H. Hou, Stochastic switching in a magnetic-tunnel-junction neuron and a bias-dependent Néel-Arrhenius model, Phys. Rev. Appl. **18**, 064034 (2022).

[52] A. Sengupta, P. Panda, P. Wijesinghe, Y. Kim, and K. Roy, Magnetic tunnel junction mimics stochastic cortical spiking neurons, Sci. Rep. **6**, 2045 (2016).

[53] Q. Zheng, X. Zhu, Y. Mi, Z. Yuan, and K. Xia, Recurrent neural networks made of magnetic tunnel junctions, AIP Adv. **10**, 025116 (2020).